

Leveraging Single-View Images for Unsupervised 3D Point Cloud Completion

Lintai Wu, Qijian Zhang, Junhui Hou, *Senior Member, IEEE*, and Yong Xu, *Senior Member, IEEE*

Abstract—Point clouds captured by scanning devices are often incomplete due to occlusion. Point cloud completion aims to predict the complete shape based on its partial input. Existing methods can be classified into supervised and unsupervised methods. However, both of them require a large number of 3D complete point clouds, which are difficult to capture. In this paper, we propose Cross-PCC, an unsupervised point cloud completion method without requiring any 3D complete point clouds. We only utilize 2D images of the complete objects, which are easier to capture than 3D complete and clean point clouds. Specifically, to take advantage of the complementary information from 2D images, we use a single-view RGB image to extract 2D features and design a fusion module to fuse the 2D and 3D features extracted from the partial point cloud. To guide the shape of predicted point clouds, we project the predicted points of the object to the 2D plane and use the foreground pixels of its silhouette maps to constrain the position of the projected points. To reduce the outliers of the predicted point clouds, we propose a view calibrator to move the points projected to the background into the foreground by the single-view silhouette image. To the best of our knowledge, our approach is the first point cloud completion method that does not require any 3D supervision. The experimental results of our method are superior to those of the state-of-the-art unsupervised methods by a large margin. Moreover, compared to some supervised methods, our method achieves similar performance. We will make the source code publicly available at <https://github.com/lwtu6/cross-pcc>.

Index Terms—Point cloud completion, cross-modality, single-view image, unsupervised learning.

I. INTRODUCTION

THE recent years have witnessed the thriving development of 3D sensing technology and the rapid popularization of 3D scanning equipment. As one of the most fundamental and common 3D representation modalities, point cloud data have attracted increasing interests from both industry and academia and played a key role in a variety of downstream applications, such as autonomous driving [1], [2], scene understanding [3], [4], motion analysis [5], [6], and SLAM [7]. Nevertheless, in practical scenarios, directly acquiring high-quality point clouds from the output end of various 3D sensors/scanners is far from straightforward. Due to self-occlusion as well as the existence

of environmental obstacles, the captured raw point cloud data typically suffer from sparsity and incompleteness, which may significantly limit the subsequent processing pipelines and hurt downstream task performances.

To computationally address the above issues, driven by the recent advancements of 3D deep set architectures [8], [9], [10], [11], [12], there have emerged numerous deep learning-based point cloud completion frameworks that consume partial point clouds as inputs and reconstruct complete point clouds of the corresponding objects. Generally, existing research on point cloud completion can be mainly classified into *supervised* and *unsupervised* learning paradigms, in terms of *whether ground-truth partial-complete pairs are available and leveraged in the training stage*.

Architecturally, existing supervised point cloud completion frameworks [13], [14], [15], [16], [17], [18] typically adopt encoder-decoder architectures, which consume as input a partial point cloud and tend to recover its complete geometric structure at the output end. Thanks to the availability of partial-complete pairs, the training process can be directly driven by optimizing shape similarity between the reconstructed point cloud and its corresponding ground-truth complete point cloud. However, the practical applicability of these methods can be restricted due to the requirement of collecting a large amount of high-quality complete point cloud models as ground-truths, which can be demanding and time-consuming. Another representative family of unsupervised methods [19], [20], [21], [22], [23] introduce Generative Adversarial Networks (GANs) [24] to perform point cloud completion without requiring the supervisions provided by the complete shapes paired with the partial inputs during the training stage. To acquire rich prior knowledge of 3D shapes, they first leverage a large complete and clean 3D point cloud dataset from other distributions to pre-train the model, and then they use the learned prior knowledge to guide the completion of the partial inputs with the help of GANs. However, these methods still heavily rely on a large complete and clean 3D point cloud dataset that is difficult to acquire in practice, and the training of GANs is widely known to be unstable.

In addition, most previous methods use only partial point clouds as inputs. However, a single partial point cloud of an object cannot always determine its missing part. For example, given a partial point cloud of a chair with only legs, it is difficult to infer whether this chair has a back. In this case, RGB images can help us predict the complete shape since they provide compact shape information from a specific view angle.

In this paper, we use both view images and partial point

This project was supported by the Hong Kong Research Grants Council under Grant 11219422, Grant 11202320, and Grant 11218121. (*Corresponding author: Junhui Hou*)

L. Wu, Q. Zhang, and J. Hou are with the Department of Computer Science, City University of Hong Kong, Hong Kong SAR. L. Wu is also with the Bio-Computing Research Center, Harbin Institute of Technology, Shenzhen, Shenzhen 518055, Guangdong, China. Email: lintaiwu2-c@my.cityu.edu.hk; qijizhang3-c@my.cityu.edu.hk; jh.hou@cityu.edu.hk.

Y. Xu is with the Bio-Computing Research Center, Harbin Institute of Technology, Shenzhen, Shenzhen 518055, Guangdong, China, and also with the Shenzhen Key Laboratory of Visual Object Detection and Recognition, Shenzhen, Guangdong 518055, China. Email: yongxu@ymail.com.

clouds to generate the complete shapes without 3D complete point clouds as supervision. Our model consists of two stages, i.e., Coarse Shape Reconstruction (CSR) and View-assisted Shape Refinement (VSR). The CSR stage aims to generate a coarse complete point cloud based on the cross-modal features. In this stage, we use a 3D encoder to extract 3D features from a partial point cloud, and a 2D encoder to extract 2D features from a single-view image. The 3D and 2D features are then fused by a fusion module to get the global feature. In this way, the global feature takes full advantage of the information provided by both the partial point cloud and the view image. Our decoder aims to transform the global feature into a complete point cloud. Inspired by SnowflakeNet [25], we achieve this by first predicting a sparse point cloud and then splitting the points into multiple child points. The point cloud produced by the CSR stage is coarse and inaccurate. It has many outliers and some details, such as small holes and parts, are lost. To address these issues, we refine the generated point cloud in the second stage. In the VSR stage, in order to eliminate outliers, we propose a View Calibrator (VC) to move the points projected within the background into the foreground of the silhouette map binarized from the input view image. This calibrator eliminates outliers and recovers some details from a single view, but outliers from other views still exist. To further refine the results, we adopt DGCNN [26] to predict the offset of each point and use the VC to calibrate the result again.

The supervision guides the shape of predicted results. The supervised methods directly use complete and clean point clouds as supervision. The previous unsupervised methods also require a large number of complete point clouds as supervision to pre-train models for capturing prior shape information. In this paper, we only use 2D images as supervision. Specifically, inspired by the unsupervised single image-based 3D reconstruction method 2DPM [27], in the data pre-processing stage, we uniformly sample as ground truth 2D points in the foreground pixels from different views of silhouette images. In the training stage, we project the predicted point cloud to the 2D plane and compute the Chamfer Distance (CD) between the projected points and sampled points. Extensive experiments demonstrate that our method outperforms the state-of-the-art unsupervised methods by a large margin. Moreover, our method yields similar results to some supervised methods.

Conclusively, the core contributions of this paper are three-fold:

- We propose an unsupervised point cloud completion method that completely without requiring any 3D supervision. To the best of our knowledge, our work is the first one to complete point clouds without any 3D supervision. Compared to the previous unsupervised methods, our method requires only 2D images, which are easier and inexpensive to capture.
- We propose to use image features to enhance the features of 3D point clouds. We design a feature extraction and a fusion module to fuse these features of two modalities. Our model takes full advantage of both 2D images and 3D point clouds, which largely boosts the performance.
- We propose a view-assisted refinement stage to move

outliers to more correct positions and refine them with 2D images. The view calibrator in the refinement stage can effectively reduce outliers and recover details.

The remainder of this paper is organized as follows. Section II reviews the previous point cloud completion, reconstruction and single image-based 3D reconstruction approaches. Section III introduces our methods in detail. Section IV introduces our experimental settings, results and analyses. Section V summarizes our work.

II. RELATED WORK

A. 3D Point Cloud Completion and Reconstruction

1) *Supervised methods*: The supervised methods can be generally divided into two categories according to the intermediate data representations. One type is the voxel-based methods [17], [28], [29], [30]. These methods first voxelize point clouds as occupancy grids and then employ 3D convolutional neural networks (3D CNNs) architecture to process them. Dai et al. [28] used a 3D-Encoder Predictor Network to predict a coarse shape and then designed a 3D shape synthesis method to refine the coarse output with the shape prior from a complete shape database. Xie et al. [17] proposed a novel Gridding and Gridding Reverse module for converting between point clouds and voxels to reduce structural information loss. Besides, they designed a Cubic Feature Sampling module to extract context features of neighbor points. Although the voxel-based methods could take advantage of the strong ability of CNNs, the 3D CNNs require large computational costs. Also, the voxelization operation may lose the accuracy of point coordinates.

Another type is point cloud-based methods. These methods directly use point clouds as inputs and intermediate representations and employ Multi-Layer Perceptron (MLP) to extract features. There are two mainstream methods to generate missing parts of point clouds.

The first one assumes that the 3D surfaces of point clouds can be computed from the 2D manifold by consecutive mapping(folding-based methods). For example, FoldingNet [31] employed an encoder to extract the global feature of the partial point cloud and then used a 2D grid together with the global feature to reconstruct the complete point cloud by a decoder. However, the FoldingNet cannot fold a 2D grid into a complex shape. Yuan et al. [13] extended this method by first using fully-connected (FC) layers to predict a coarse point cloud and then employing the Folding operation for each coarse point. This method takes full advantage of both the flexibility of FC layers and the surface-smoothness of Folding operation. Groueix et al. [32] used multiple MLPs to deform 2D grids into different local patches. Although this method can generate more complex shapes than FoldingNet, there are some overlapped regions between patches. In order to solve this problem, Liu et al. [14] proposed an expansion penalty to reduce the overlap areas. Tang et al. [33] used multiple grids to generate a point cloud with shared MLP. They designed a Stitching loss to preserve the uniformity of points. Wen et al. [16] proposed a skip-attention module to capture the geometric information of local regions and used the Folding operation to generate the complete point cloud hierarchically. Rather than

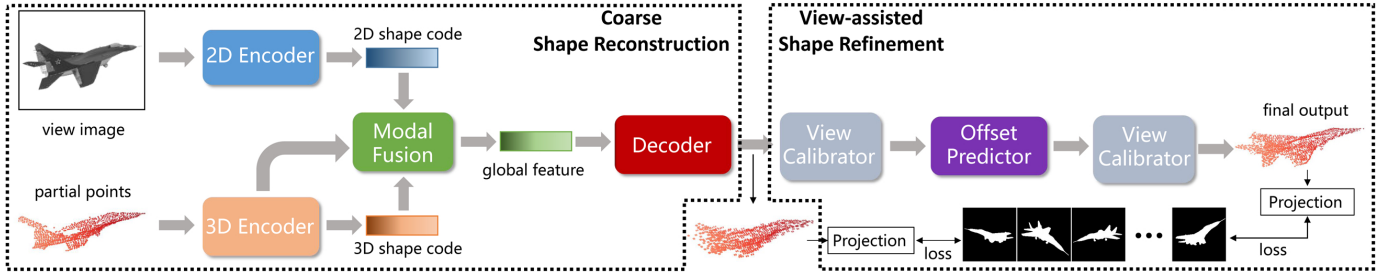


Fig. 1. Flowchart of the proposed Cross-PCC. The Cross-PCC comprises two stages, i.e., Coarse Shape Reconstruction (CSR) and View-assisted Shape Refinement (VSR). The CSR stage consists of a 3D encoder, a 2D encoder, a modality fusion module and a decoder. The VSR stage is composed of two view calibrators and an offset predictor.

utilizing the fixed 2D grid as seeds, Yang et al. [34] used a network to learn a high-dimension seed to generate point clouds. Similarly, Pang et al. [35] argued that the fixed 2D grid cannot capture the complex topologies of point clouds. They used a network to learn the point cloud topology and tore the grid into patches to fit the object shape. Yu et al. [15] considered the point cloud completion as a translation task and employed the Transformer to infer the missing parts based on the given parts. They first generated coarse missing points and then used the Folding operation to generate their neighbor points.

The main drawback of the folding-based methods is that they predefine a topology for the target object, which constrains the generated complete shape. Therefore, some approaches directly generated points in 3D space (point-based methods) instead of by 2D-manifold. Tchampi et al. [36] designed a rooted-tree decoder to generate points hierarchically as the tree grows. Inspired by the generation process of snowflakes, Xiang et al. [25] proposed to split each parent point into several child points in a coarse-to-fine manner. Besides, they proposed a skip-transformer block to capture the relation between the features of child points and parent points.

Recently, the multimodal fusion of point clouds and images has been proven effective in many tasks. For example, in the 3D object detection task, the performance of Lidar and image fusion-based methods usually surpass that of single modal methods [37], [38], [39]. Some researchers have begun to make use of 2D images to help the completion of point clouds.

Intuitively, the RGB image can provide information about occupancy and emptiness. To utilize the emptiness information, Gong et al. [40] used MLPs to encode both partial input and emptiness ray generated from depth images and then refine the predicted complete point cloud under the guidance of the emptiness. This method can distinguish the boundary of the point cloud well. Zhang et al. [18] adopted a single view image to predict a coarsely complete point cloud and proposed a Dynamic Offset Predictor to refine the coarse output. However, directly predicting a complete point cloud from an image is difficult and inaccurate. More importantly, this method is a supervised learning framework, and it is non-trivial to adapt it to our unsupervised setting that lacks complete point clouds as ground truth.

2) *Unsupervised methods*: The existing unsupervised point cloud completion methods aim to estimate the complete point cloud of a partial point cloud in an unpaired manner. They do not require the supervision provided by the complete shapes paired with the partial inputs during the training stage. Instead, they require a large dataset of complete and clean point clouds to train a model to capture the prior 3D shape information. Then they leveraged the pre-trained model to guide the completion of the partial point cloud.

Chen et al. [19] proposed the first unsupervised point cloud method. They first pre-trained two Auto-encoders by reconstructing partial inputs and complete point clouds, respectively. The partial inputs and complete point clouds are from different data distributions. Then they used a generator to transform the global feature of the partial input and a discriminator to differentiate between the transformed global feature and that of the complete point clouds. By making the global feature of partial input close to the complete one, the completion results are more reasonable. Wen et al. [20] extended this method by simultaneously learning the transformation from partial inputs to complete point clouds and its inverse transformation to enhance the 3D shape understanding ability of the model. Zhang et al. [21] introduce the GAN Inversion to the point cloud completion task. They first pre-trained a GAN with a complete and clean dataset. Then they searched for a global feature (latent code) that was best matched with the partial input in the latent space of GAN and optimized it. Cai et al. [22] proposed to learn a unified latent space for partial and complete point clouds by modeling the incompleteness as the occlusion degree of the global feature of complete point clouds. The model is capable of well understanding the complete shape by being trained on the unified latent space. The advantage of these methods is the strong generation ability. Since the pre-trained Auto-encoders and latent codes contain information of many 3D shapes, the model can generate many reasonable shapes when inputting a new partial point cloud from different data distributions. However, they require a large complete 3D point cloud dataset. Although these data are unpaired with the input partial point cloud, capturing 3D data is expensive and inconvenient. Besides, the training of GAN is difficult and time-consuming.

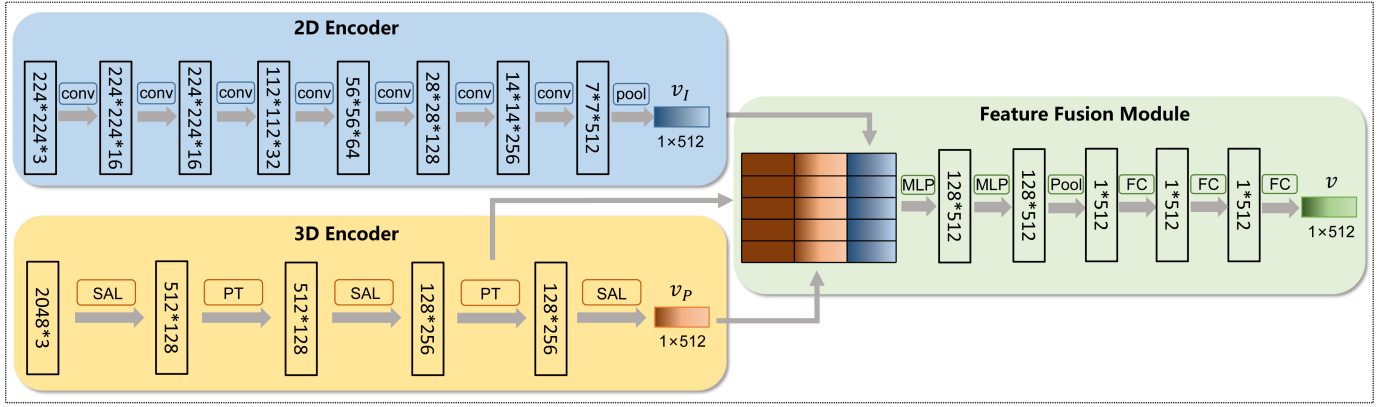


Fig. 2. Architecture of 2D encoder, 3D encoder and modality fusion module. “SAL” and “PT” denote Set Abstraction Layer in PointNet++ [9] and Point Transformer [25], [41], [42], [43].

B. Single Image-based 3D Reconstruction

Single image-based 3D reconstruction targets to predict the 3D shape from the single-view image. Here, we briefly review the unsupervised methods for point cloud representation since they are more related to our work.

Without 3D supervision, the unsupervised methods usually use differentiable renderers to render the generated point cloud into a silhouette or RGB image and then compare the similarity of the rendered and ground truth image [44], [45], [46], [47], [48], [49], [50], [51]. They first project the 3D points to the image plane under the given camera parameters and then compute the influence of each point on the pixel’s color of the target image. The color of each pixel is determined by the influences and depth values of all projected points.

The rendering process consumes a lot of computational time. To reduce the computation cost while keeping the performance, some researchers only project 3D points to the image plane, and then utilize silhouette images to constrain the positions of the projected points. We refer to these methods as projection-based methods. For example, Han et al. [52] designed a smooth silhouette loss to pull the projected points inside the foreground of the silhouette image, and a repulsion loss to make the projected points cover the entire foreground. To recover detailed structures of 3D shapes, Chen et al. [27] proposed to uniformly sample a fixed number of 2D points within the silhouettes regardless of the image resolution, and then computed the Chamfer Distance between the projected and sampled points to supervise the generated shapes. Extensive experimental results demonstrate that the projection-based methods are effective and require less computational cost than the rendering-based methods.

III. PROPOSED METHOD

Denote by $P_{in} \in \mathbb{R}^{N \times 3}$ the partial point cloud of an object and $V \in \mathbb{R}^{W \times H \times 3}$ an RGB image captured from a random view angle, where N is the number of points, W, H are the width and height of the image. Our goal is to find a mapping $f(P_{in}, V) = P_{out}$, where P_{out} denotes the complete point cloud of the partial input.

As depicted in Figure 1, our approach consists of two stages, i.e., Coarse Shape Reconstruction (CSR) and View-assisted

Shape Refinement (VSR). In the CSR stage, we predict a coarse complete point cloud based on the partial point cloud and a view image. In the VSR stage, we propose a view calibrator and an offset predictor to refine the coarse point cloud. In what follows, we will introduce the proposed method in detail.

A. Coarse Shape Reconstruction

The CSR stage contains a 3D encoder, a 2D encoder, a modality fusion module and a decoder. The detailed architecture is shown in Figure 2. The 3D encoder extracts a 3D shape code representing the 3D global shape from the partial point cloud. It comprises three Set Abstraction Layers [9] and two Point Transformer Layers [25], [41], [42], [43]. The Point Transformer Layers aim to capture the correlation between point features. The 2D encoder extracts a 2D shape code representing the 2D global shape from the view image. It is composed of eight convolution layers and a global pooling layer. To fuse these two-modality features while capturing both the local and global shape information, we concatenate the intermediate 3D local feature, 2D and 3D shape codes, and then use MLPs to encode them into a global feature. To further enhance the global feature, we employ three Fully-Connected (FC) layers to embed it. We term this module the “modality fusion module”.

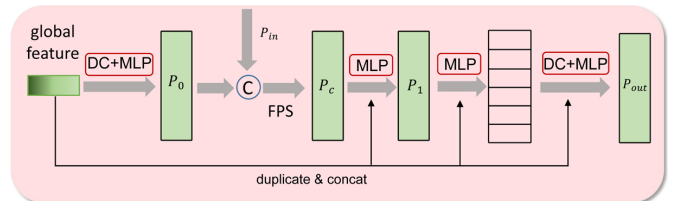


Fig. 3. Architecture of the decoder. “DC” denotes the “Deconvolution” operation. “C” in the circle means concatenation operation.

The decoder should predict the complete shape while preserving the partial inputs. Inspired by [25], we first predict a coarse point cloud and then split each point into several child points to generate detailed parts by MLPs. The architecture of the decoder is shown in Figure 3. Specifically, we employ a

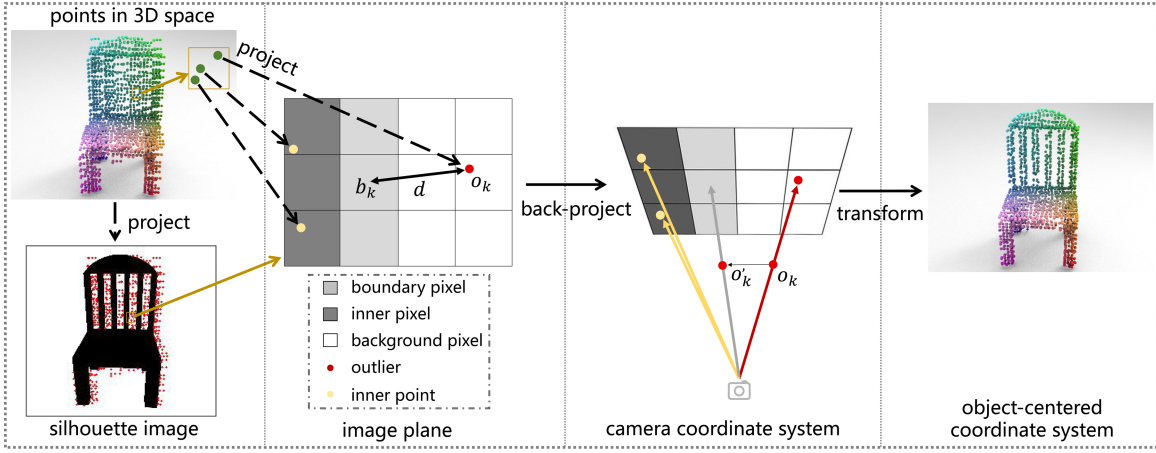


Fig. 4. Illustration of the calibration operation. We project the predicted points in 3D space into the image plane and then replace the x and y coordinates of the outlier with those of its nearest boundary pixel. In the camera coordinate system in which all the points in the image plane are rays starting from the camera, this procedure means moving the outlier to the ray of its nearest boundary pixel.

deconvolution layer and four layers of MLPs to transform the global feature v into the coarse point cloud $P_0 \in \mathbb{R}^{N_0 \times 3}$. In order to better preserve the partial input, we concatenate the partial input P_{in} and P_0 and adopt the Farthest Point Sampling (FPS) method to sample N_c points to obtain $P_c \in \mathbb{R}^{N_c \times 3}$. Since the points sampled from P_{in} and P_0 may be inconsistent in density and shape, we feed P_c together with the global feature to MLPs to obtain a refined point cloud $P_1 \in \mathbb{R}^{N_c \times 3}$. Next, we embed P_1 into point features and then use a deconvolution layer to split each point feature into r child features. The split operation aims to infer r neighbors' positions of each point in P_1 to get a finer point cloud. Finally, we use MLPs to decode these child features to obtain the final complete output $P_{out} \in \mathbb{R}^{N \times 3}$.

B. View-assisted Shape Refinement

The coarse point cloud predicted by the CSR stage contains many points lying outside the object boundaries. As Figure 4 shows, these points lie in the background of the silhouette images when projected into the image plane (we call these out-of-boundary points outliers and others inner points). We propose a View Calibrator (VC) to calibrate these outliers with the help of the single-view silhouette image. Specifically, given a point cloud $P \in \mathbb{R}^{N \times 3}$ and an RGB view image S from a random view angle, we first binarize the input view image to obtain a silhouette image. And then we find the coordinates of all the boundary pixels $B \in \mathbb{R}^{L \times 2}$ of the silhouette image by [53], where L is the number of boundary pixels. Next, we project P into the image plane by employing the intrinsic and extrinsic camera parameters $T \in \mathbb{R}^{4 \times 4}$. Let the projected point set be $P' = (\mathbf{x}', \mathbf{y}', \mathbf{z}')$, and the projection can be formulated as

$$(\mathbf{x}', \mathbf{y}', \mathbf{z}', \mathbf{1})^T = T * (\mathbf{x}, \mathbf{y}, \mathbf{z}, \mathbf{1})^T, \quad (1)$$

Then we determine outliers and inner points according to the silhouette image. Let $O \in \mathbb{R}^{K \times 3}$ be the outlier set in P' , i.e., $O \subset P'$, where K is the number of outliers. Since the pixel value for background is 0 and foreground is 1 in the

silhouette images, the j -th project point $p'_j = (x'_j, y'_j, z'_j) \in O$ if $S(\lfloor x'_j, y'_j \rfloor) = 0$.

In the next step, for each outlier $o_k = (x_k, y_k, z_k) \in O$, we compute the Euclidean distance between it and all boundary pixels in the image plane without z -axis and select the nearest boundary pixel $b_k = (x_{b_k}, y_{b_k})$. That is:

$$b_k = \operatorname{argmin} d(o_k, B), \quad (2)$$

where $b_k \in B$, $d(\cdot, \cdot)$ means the Euclidean distance of two points. Then we replace the x and y coordinates of o_k with the counterparts of b_k . The new coordinate of o_k is $o'_k = (x_{b_k}, y_{b_k}, z_k)$. That means we move the outliers inside the foreground in the silhouette image while keeping the z coordinate unchanged. Finally, we back-project the new point set o'_k into the object-center coordinate by:

$$(\mathbf{x}_{cal}, \mathbf{y}_{cal}, \mathbf{z}_{cal}, \mathbf{1})^T = T^{-1} * (\mathbf{x}', \mathbf{y}', \mathbf{z}', \mathbf{1})^T, \quad (3)$$

where $(\mathbf{x}_{cal}, \mathbf{y}_{cal}, \mathbf{z}_{cal}) = P_{cal}$ represents the calibrated point set. Figure 4 illustrates the whole procedure.

The VC eliminates outliers and recovers some details from a single view. On the one hand, however, outliers from other views still exist. On the other hand, the calibration may affect the density of the points. To further adjust the positions of the calibrated points, we use DGCNN [26] as the offset predictor to infer the offset for each point. The DGCNN may generate some outliers due to the limited capability of neural networks. To address this issue, we utilize the VC to move the outliers again.

C. Loss Function

There are some 3D reconstruction approaches using 2D images as supervision. Considering both the effectiveness and computational cost, we employ the projection-based method proposed by Chen et al. [27]. We assume that each object has I RGB view images captured from different view angles. In the data-preprocessing stage, we binarize these RGB images to obtain silhouette images. And then we uniformly sample M 2D points $Q_i \in \mathbb{R}^{M \times 2}$ in the foreground pixels of each

silhouette image, where $i = 1, 2, \dots, I$. During the training stage, for the predicted point cloud P , we project it into the i -th image plane and the result is denoted as P'_i . Then we compute the 2D Chamfer Distance (CD) between the sampled points Q_i and P'_i .

$$CD(Q_i, P'_i) = \frac{1}{|Q_i|} \sum_{q_i \in Q_i} \min_{p'_i \in P'_i} \|q_i - p'_i\| + \frac{1}{|P'_i|} \sum_{p'_i \in P'_i} \min_{q_i \in Q_i} \|p'_i - q_i\|. \quad (4)$$

For each object, we compute the CD loss for all views and aggregate them. Our projection loss is given as below.

$$L_{proj}(Q, P') = \frac{1}{I} \sum_{i=1}^I CD(Q_i, P'_i). \quad (5)$$

In addition, to preserve the partial input, we also employ the partial matching loss [20]. It computes the unidirectional CD from output to input.

$$L_{part}(P_{in}, P) = \frac{1}{|P_{in}|} \sum_{p_{in} \in P_{in}} \min_{p \in P} \|p_{in} - p\|. \quad (6)$$

Our total loss function is given as below.

$$L_{total} = L_{proj}(Q, P'_0) + L_{part}(P_{in}, P_0) + L_{proj}(Q, P'_1) + L_{part}(P_{in}, P_1) + L_{proj}(Q, P'_{out}) + L_{part}(P_{in}, P_{out}), \quad (7)$$

where P'_0, P'_1, P'_{out} are the 2D points projected by P_0, P_1, P_{out} .

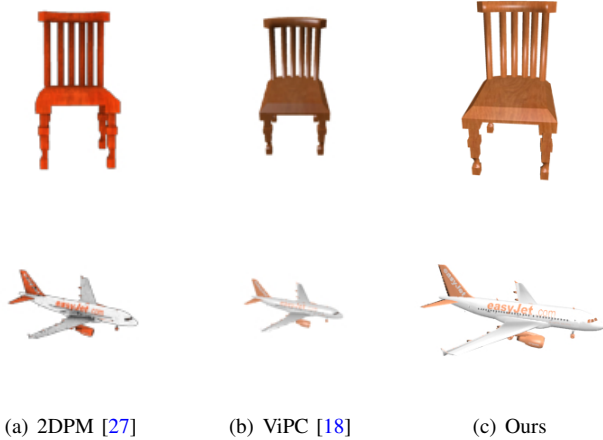


Fig. 5. Comparison between our rendered images and the existing rendered images. Note that all the images are shown at the same size. The images provided by 2DPM [27] are too unreal, and the rendered objects in the images of ViPC [18] are too small. In contrast, our renderer images are more real and the objects are larger so as to keep more details and reduce the background pixels.

IV. EXPERIMENTS

A. Dataset and Evaluation Metric

To better evaluate our method, we experiment on both synthetic data and real-world data. For the synthetic point clouds, we use the PCN dataset [13] and the 3D-EPN dataset

[28] provided by PCL2PCL [19]. In both datasets, each object contains eight partial point clouds, which are generated by back-projecting depth images of eight view angles into 3D space. We set the number of partial points to 2048 by upsampling or downsampling. The point numbers of complete shapes in 3D-EPN and PCN are 2048 and 16384, respectively.

For the view images, as Figure 5 shows, the existing rendered RGB images are either too unreal [27], [52], [54] or the objects in the images are too small [18], [55], which may lose some details and waste many convolutional parameters to compute the background pixels. To acquire high-quality image data, we re-render RGB images from ShapeNet [56] by Blender¹. The image size is $224 \times 224 \times 3$. We set the object covers the largest space in the image while keeping all foreground pixels within the image boundary. For each object, we render eight RGB images from different view angles. Specifically, we sample 4 angles uniformly along the y-axis, and one angle each along the x-axis in the positive and negative directions.

The evaluation metric we employ for synthetic scans is Chamfer Distance. Considering that each object contains eight view images captured from different view angles, we report two kinds of metrics named CD_{min} and CD_{avg} . Specifically, CD_{min} computes the minimum CD from all view images of each object. It measures which view image of an object can generate the best point cloud. CD_{avg} computes the average CD among all view images of each object. The formulas of the CD_{min} and CD_{avg} are listed as follows.

$$CD_{min} = \frac{1}{J} \sum_{j=1}^J \min_{i=1, \dots, I} CD(Pred(j, i), GT(j)), \quad (8)$$

$$CD_{avg} = \frac{1}{I \times J} \sum_{j=1}^J \sum_{i=1}^I CD(Pred(j, i), GT(j)),$$

where J denotes the number of objects, and I represents the number of view images for each object.

For the real-world dataset, we use KITTI [57] which contains both the raw point clouds and RGB scene images. Following the previous works [19], [21], we only test our model on the car category. For partial point clouds, we extract the car objects with more than 100 points in the Velodyne data. For the view images, we crop and segment the cars in the images provided by KINS [58]. The car images are captured from different view angles. In the raw images of KITTI, the cars vary in size and occlusion degree. To acquire high-quality view images, considering both the completeness of the objects and image resolutions, we only select the cars whose lengths of bounding boxes are larger than 100 pixels and are not occluded by other objects. Totally, we get 156 car images and partial point clouds. Since there are no complete point clouds in KITTI, following the previous papers [13], [19], [21], [15], we employ the Minimal Matching Distance (MMD) as our evaluation metric when evaluating our model on KITTI. The MMD is the minimum CD between each predicted result and the complete car point clouds from the ShapeNet. It measures the similarity between the predicted shape and typical cars.

¹<https://www.blender.org/>

B. Implementation Details

The point numbers of P_{in} , P_0 , P_c , P_1 , P_{out} are 2048, 256, 512, 512 and 2048, respectively. The upsampling rate r is 4. The number of the sampled 2D points M is 4096. We used Adam optimizer to train our model. The batch size is 32. The initial learning rate is $1e-4$. The learning rate exponentially decays by 0.7 for every 10 epochs in the CSR stage and exponentially decays by 0.1 for every 10 epochs in the VSR stage. It takes 200 and 50 epochs to converge for the CSR stage and VSR stage, respectively. For a fair comparison, we train a separate model for each category following the unsupervised methods. The training process is conducted on an NVIDIA RTX 3090 GPU with Intel(R) Xeon(R) CPUs.

C. Comparison with State-of-the-Art Methods

1) *Results on synthetic data:* We first conduct experiments on two widely-used synthetic benchmarks, i.e., 3D-EPN and PCN. Table I shows the quantization results of our method and other state-of-the-art methods, including supervised methods (3D-EPN [28], FoldingNet [31], PCN [13], TopNet [36], SnowflakeNet [25]) and unsupervised methods (PCL2PCL [19], Cycle [20], Inversion [21]). We can see that the results of our methods surpass the previous unsupervised methods by a large margin. Specifically, compared with the previous best unsupervised method Cycle, the results of our method are reduced by 4.6/3.9 in terms of the average CD_{min} and CD_{avg} among all categories. Especially, our results under the ‘‘lamp’’ and ‘‘table’’ categories surpass the best unsupervised results by 15.2/13.7 and 11.3/10.2, respectively. Besides, compared to the supervised methods, although our method still falls behind the latest state-of-the-art method SnowflakeNet [25] by a relatively large margin, we achieve results that are extremely close to those of some supervised methods, i.e., FoldingNet, PCN, TopNet. The average CD gap between our and these methods is less than 0.8/1.5. Moreover, our method even outperforms these methods under some categories. For example, on the lamp category, the CD_{min}/CD_{avg} of our method is lower than PCN by 5.2/3.7.

The quantitative results on the PCN benchmark are shown in Table II. Compared to the best unsupervised method, our method improves the completion performance by 4.9/4.2 in terms of the CD_{min} and CD_{avg} . Especially, our method reduces the CD on the ‘‘Lamp’’ and ‘‘Table’’ categories by 7.5/6.3 and 8.1/7.0, respectively. In addition, the results of our method are very close to those of some supervised methods with a minimum gap of 1.5/2.2 in terms of the averaged CD. On the ‘‘Lamp’’ and ‘‘Table’’ categories, the CD results of our method exceed the FoldingNet, PCN, and TopNet by 4.8/3.6, 2.5/1.3 and 4.3/3.1, respectively.

Figure 6 shows the qualitative results of our method and the state-of-the-art methods on the synthetic dataset. From Figure 6, we can see that our method can effectively recover the missing part while preserving the partial input. Both the supervised and unsupervised methods are apt to alter the partial input and thus generate a shape with a large difference from the input and ground truth. Our method, however, preserves the input shape completely. In addition, the supervised and unsupervised

methods do poor in recovering some details, such as holes and thin bars. For example, these methods fill the hollows in the backs of the chair and couch in Figure 6, which is inconsistent with the ground truth. In contrast, our method accurately predicts the bars and holes.

2) *Results on real-world scans:* Our completion model can be extended to real-world scans. We test our models on KITTI data which are extracted from real-world scenes. Table III shows the quantization results of our model and other state-of-the-art methods, including supervised and unsupervised methods. Compared with the latest unsupervised methods, our method yields the best result in terms of MMD. And our method is comparable with some supervised methods with a little behind. These results demonstrate that our model is capable of predicting reasonable complete cars according to the sparse and partial point clouds. Figure 7 shows some visual results of our methods and two unsupervised methods, i.e., Cycle [20] and Inversion [21]. We can find that our model can predict reasonable shapes while doing better in preserving the partial input compared with the unsupervised methods.

D. Ablation Study

1) *Effect of each component:* To analyze the effectiveness of three key components of our model, i.e., the image feature branch (2D encoder and modality fusion module), view calibrator and offset predictor, we conduct ablation studies on the 3D-EPN benchmark. The experimental settings are consistent with Section IV-C1.

As Table IV shows, without any components, the model yields poor results. After adding the 2D encoder, the model reduces the average CD by 1.9/1.4. It proves that our 2D encoder and modality fusion module can extract useful 2D features from images and fuse them with point cloud features effectively.

Further, after embedding our calibrator behind the generation decoder and offset predictor, we improve the results by 0.9/0.6 and 0.1/0.1, respectively. After the calibrated point clouds are refined by the offset predictor, the average CD decreases significantly by 2.0/2.1. It means that the offset predictor can predict more precise coordinates for calibrated points.

To better evaluate the effect of our VSR stage, as shown in Figure 8, we visualize some results with or without refinement from two different angles. From Figure 8 (d) and (g), we can see that the CSR stage outputs many outliers around the object. Figure 8 (e) and (h) illustrates that the VSR stage effectively moves most of the outliers to accurate positions.

2) *Effect of view angles of the input images:* Our model consumes a single-view image as input to aid the completion. Intuitively, the images captured from different angles may affect the completion results differently. To verify the effect of view angles, we first compute the standard deviations of CD values of the results predicted by eight view images for all objects. The formula of this metric is listed below.

$$Std = \frac{1}{J} \sum_{j=1}^J \sqrt{\frac{1}{I} \sum_{i=1}^I (CD_{j,i} - \overline{CD}_j)^2}, \quad (9)$$

TABLE I

RESULTS ON 3D-EPN BENCHMARK IN TERMS OF L2 CD \downarrow (SCALED BY 10^4). NOTE THAT THE VALUES TO THE LEFT AND RIGHT OF THE SLASH “/” ARE THE CD $_{min}$ AND CD $_{avg}$, RESPECTIVELY. THE **BOLD** NUMBER REPRESENTS THE BEST RESULT OF THE UNSUPERVISED METHODS.

Methods	Supervised	Average	Plane	Cabinet	Car	Chair	Lamp	Couch	Table	Watercraft
3D-EPN [28]	yes	29.1	60.0	27.0	24.0	16.0	38.0	45.0	14.0	9.0
FoldingNet [31]	yes	8.2	2.7	8.7	5.0	9.8	14.5	8.7	9.7	7.1
PCN [13]	yes	7.6	2.0	8.0	5.0	9.0	13.0	8.0	10.0	6.0
TopNet [36]	yes	7.8	2.5	8.5	4.6	9.1	13.9	8.8	9.1	6.5
SnowflakeNet [25]	yes	5.0	1.4	6.3	4.0	6.1	6.2	6.3	6.5	3.4
PCL2PCL [19]	no	17.4	4.0	19.0	10.0	20.0	23.0	26.0	26.0	11.0
Cycle [20]	no	13	3.58	12.0	7.4	14.6	23.5	14.3	20.9	8.1
Inversion [21]	no	18.3	5.1	21.9	12.2	21.6	24.2	20.0	31.7	9.8
Cross-PCC (ours)	no	8.4/9.1	2.3/2.4	13.0/14.0	7.4/7.6	9.8/10.6	7.8/9.3	11.5/12.1	9.6/10.7	6.1/6.8

TABLE II

RESULTS ON PCN BENCHMARK IN TERMS OF L2 CD \downarrow (SCALED BY 10^4). NOTE THAT THE VALUES TO THE LEFT AND RIGHT OF THE SLASH “/” ARE THE CD $_{min}$ AND CD $_{avg}$, RESPECTIVELY. THE **BOLD** NUMBER REPRESENTS THE BEST RESULT OF THE UNSUPERVISED METHODS.

Methods	Supervised	Average	Plane	Cabinet	Car	Chair	Lamp	Couch	Table	Watercraft
FoldingNet [31]	yes	7.7	2.4	8.4	4.9	9.2	11.5	9.6	8.4	7.4
PCN [13]	yes	7.5	3.0	7.5	5.7	9.7	9.2	9.5	9.2	6.2
TopNet [36]	yes	7.3	2.3	8.2	4.7	8.6	11.0	9.3	8.0	6.3
SnowflakeNet [25]	yes	4.5	1.3	6.7	4.3	5	4.3	6.8	4.4	3.6
Cycle [20]	no	14.4	4.1	14.2	9.9	14.6	19.2	27.8	16.8	9.0
Inversion [21]	no	14.1	3.9	17.4	11.0	13.8	14.2	23.0	20.3	9.7
Cross-PCC (ours)	no	9.2/9.9	2.5/2.8	13.9/14.7	10.6/11.1	11.7/12.4	6.7/7.9	13.5/14.3	8.7/9.8	6.1/6.9

TABLE III

RESULTS ON KITTI DATASET IN TERMS OF MMD \downarrow (SCALED BY 10^4). “VSR” DENOTES THE VIEW-ASSISTED SHAPE REFINEMENT STAGE. THE **BOLD** NUMBER REPRESENTS THE BEST RESULT OF THE UNSUPERVISED METHODS.

Methods	FoldingNet [31]	PCN [13]	TopNet [36]	Cycle [20]	Inversion [21]	Cross-PCC w/o VSR	Cross-PCC
Supervised	yes	yes	yes	no	no	no	no
MMD	6.9	6.7	7.3	9.0	10.0	10.8	8.5

TABLE IV

RESULTS COMPARISON OF OUR IMAGE FEATURE BRANCH, VIEW CALIBRATOR AND OFFSET PREDICTOR. \checkmark AND \times REPRESENTS THE MODEL WITH OR WITHOUT THE COMPONENT, RESPECTIVELY. ‘IFB’, ‘VC’ AND ‘OP’ REPRESENT THE IMAGE FEATURE BRANCH, VIEW CALIBRATOR AND OFFSET PREDICTOR, RESPECTIVELY. THE RESULTS ARE REPORTED ON THE 3D-EPN DATASET.

Component				Datasets								
IFB	1st VC	OP	2nd VC	Average	Plane	Cabinet	Car	Chair	Lamp	Couch	Table	Watercraft
\times	\times	\times	\times	13.3	3.5	19.5	11.7	15.0	14.0	16.6	17.3	9.3
\checkmark	\times	\times	\times	11.4/11.9	3.3/3.3	16.1/17.3	11.4/11.5	12.5/12.8	10.6/11.9	14.8/15.1	14.8/15.3	7.8/8.5
\checkmark	\checkmark	\times	\times	10.5/11.3	2.8/3	15.9/17.1	10.7/11.0	11.5/12.2	9.1/10.7	14.2/14.7	13.2/14.3	7.3/8.1
\checkmark	\checkmark	\checkmark	\times	8.5/9.2	2.3/2.5	13.1/14.1	7.4/7.7	10.0/10.7	7.9/9.4	11.7/12.2	9.8/10.8	6.1/6.9
\checkmark	\checkmark	\checkmark	\checkmark	8.4/9.1	2.3/2.4	13.0/14.0	7.4/7.6	9.8/10.6	7.8/9.3	11.5/12.1	9.6/10.7	6.1/6.8

TABLE V

STANDARD DEVIATIONS OF CD VALUES OF EIGHT VIEW IMAGES. THIS METRIC MEASURES THE IMPACT OF VIEW ANGLES OF INPUT IMAGES ON COMPLETION RESULTS. A LOWER VALUE MEANS LOWER IMPACT. “CSR” AND “VSR” DENOTE THE COARSE SHAPE RECONSTRUCTION STAGE AND VIEW-ASSISTED SHAPE REFINEMENT STAGE, RESPECTIVELY.

Category	Average	Plane	Cabinet	Car	Chair	Lamp	Couch	Table	Watercraft
CSR	0.390	0.021	0.792	0.039	0.262	0.967	0.177	0.377	0.487
VSR	0.525	0.106	0.670	0.154	0.481	1.178	0.373	0.698	0.537

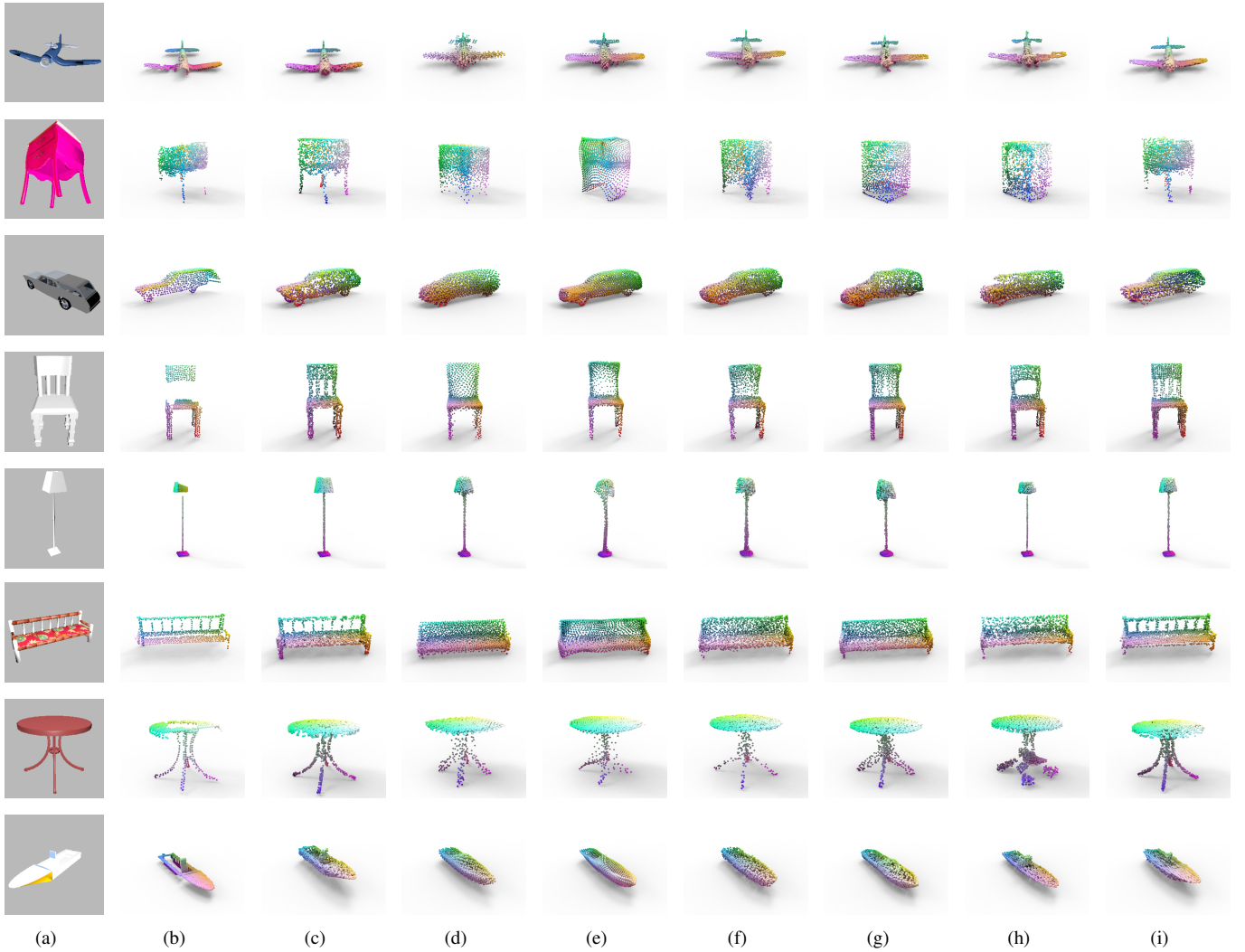


Fig. 6. Comparison of the visual results by different methods on the synthetic dataset. Note that we change the background color of the view images in our dataset from black to grey for better visualization. (a) Input image (b) Partial points. (c) Ground truth. (d) PCN [13]. (e) FoldingNet [31]. (f) TopNet [36]. (g) Cycle [20]. (h) Inversion [21]. (i) Ours

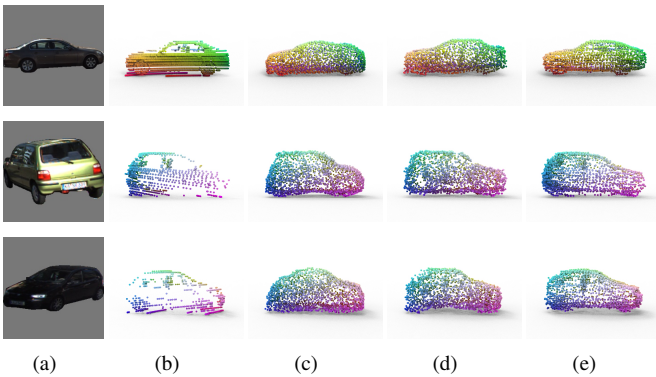


Fig. 7. Comparison of visual results between our methods and unsupervised methods on the KITTI dataset. (a) Input image (b) Input partial points. (c) Cycle [20]. (d) Inversion [21]. (e) Ours.

where J denotes the number of objects, and $\overline{CD_j}$ means the average CD of the results from I view images of the j -th object. Table V lists the standard deviation of each category.

From Table V, we can find that the view angles have a larger impact on the results of the VSR stage than the CSR stage, which demonstrates that the view calibrator more requires a suitable view angle. The standard deviations of most categories are less than 0.6, which means the results generated by images from different view angles are similar. However, the standard deviation of the “lamp” is much larger than those of others. To further study the effect of view angles of images on our results, we visualize some typical outputs with large CD standard deviations in Figure 9. Figure 9 (c) shows that the predicted outliers often populate around the thin bars and holes, such as the legs of the table and the line of the lamp. From Figure 9 (d)~(k) we can see that the view images whose results have smaller CD values always capture the parts where outliers populate. Besides, the two sub-figures in the first line of Figure 9 (j) and (k) illustrate that the view images cannot yield good results if the outliers occlude the body of the object. This is because the outliers in the 3D space will lie in the foregrounds when projected into the image plane in this case. That means they are not outliers and thus will not be calibrated. Generally,

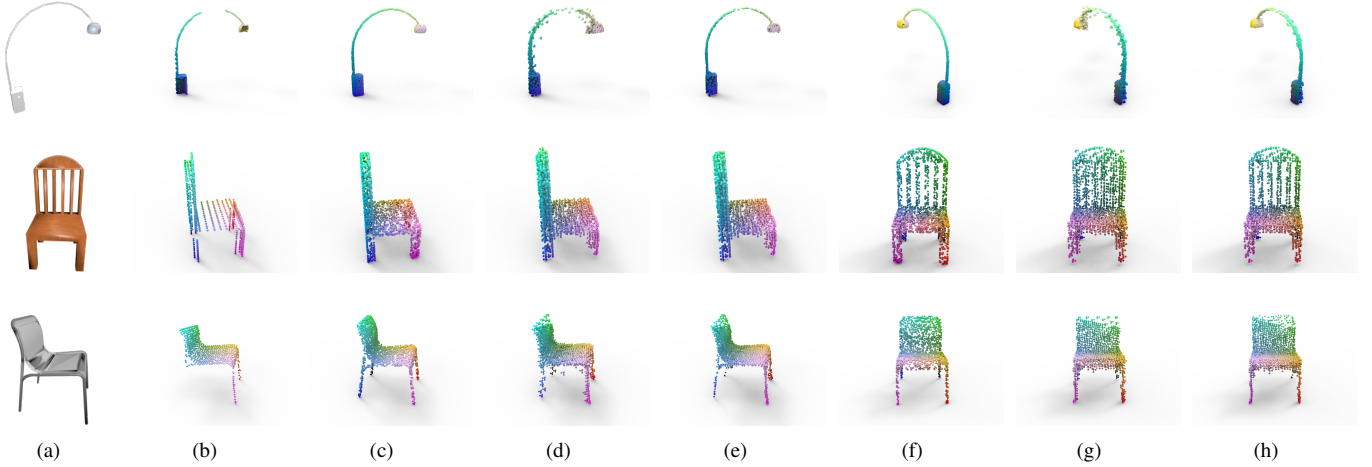


Fig. 8. Visual results of our VSR stage. (a) Input view images. (b) Input partial points. (c) Ground truth from the first view angle. (d) Predicted results without refinement from the first view angle. (e) Predicted results with refinement from the first view angle. (f) Ground truth from the second view angle. (g) Predicted results without refinement from the second view angle. (h) Predicted results with refinement from the second view angle.

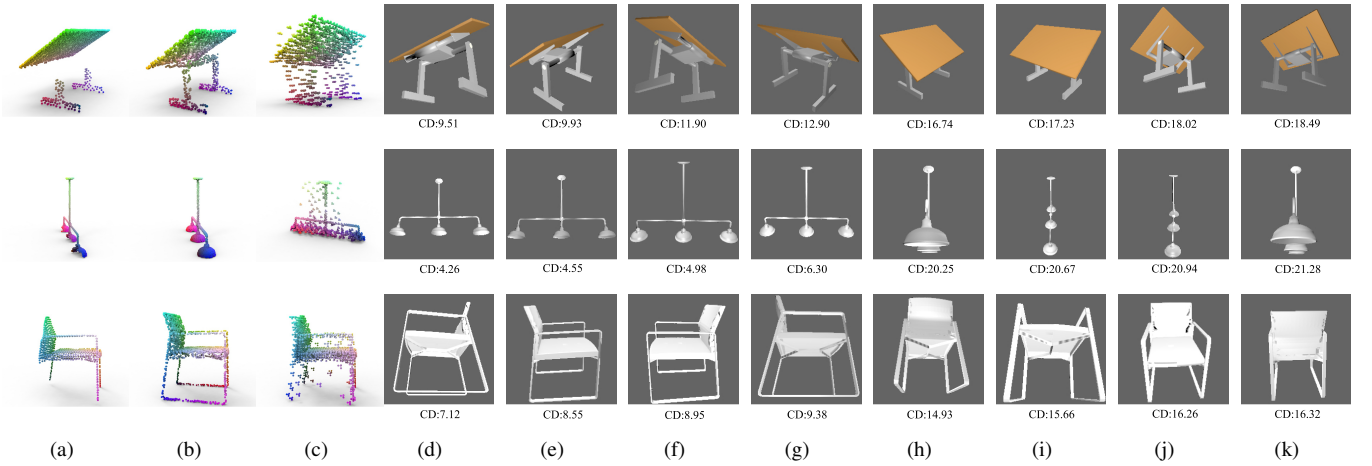


Fig. 9. Ranking of CD values of the results predicted by different view images. (a) Input partial points (b) Ground truth. (c) Predicted results without refinement. (d)~(k) CD rank of predicted results with refinement when inputting different angles of view images.

for those objects with many thin bars, holes or gaps, we should capture these parts in view images to obtain better results.

V. CONCLUSION

In this paper, we have proposed Cross-PCC, the first model to complete partial point clouds without any complete 3D ground truth. In contrast to previous methods that require a large complete and clean 3D dataset, we only leveraged 2D view images to guide the completion process. Cross-PCC consumes a partial point cloud and a single-view image as inputs and uses different views of silhouette images to constrain the predicted shape. Considering that the single modality of partial point clouds cannot always determine the unknown parts, we extracted image features and fuse them with 3D features to aid the prediction of the complete shapes. To reduce the outliers in the predicted results, we proposed a calibrator to move the outliers to correct positions and then employ an offset predictor to refine them. We conducted extensive experiments on both synthetic data and real-world data. The

experimental results show that our method outperforms state-of-the-art unsupervised methods by a large margin and only falls behind some supervised methods by a tiny gap.

REFERENCES

- [1] S. Kato, S. Tokunaga, Y. Maruyama, S. Maeda, M. Hirabayashi, Y. Kit-sukawa, A. Monroy, T. Ando, Y. Fujii, and T. Azumi, "Autoware on board: Enabling autonomous vehicles with embedded systems," in *Proc. Int. Conf. Cyber-Phys. Syst.*, 2018, pp. 287–296.
- [2] Y. Cui, R. Chen, W. Chu, L. Chen, D. Tian, Y. Li, and D. Cao, "Deep learning for image and point cloud fusion in autonomous driving: A review," *IEEE Trans. Intell. Transp. Syst.*, vol. 23, no. 2, pp. 722–739, 2021.
- [3] H. Liu, Y. Guo, Y. Ma, Y. Lei, and G. Wen, "Semantic context encoding for accurate 3d point cloud segmentation," *IEEE Trans. Multimedia*, vol. 23, pp. 2045–2055, 2020.
- [4] H. Zhu, J. Deng, Y. Zhang, J. Ji, Q. Mao, H. Li, and Y. Zhang, "Vpfnnet: Improving 3d object detection with virtual point based lidar and stereo data fusion," *IEEE Trans. Multimedia*, 2022.
- [5] Y. Wu, D. Kong, S. Wang, J. Li, and B. Yin, "An unsupervised real-time framework of human pose tracking from range image sequences," *IEEE Trans. Multimedia*, vol. 22, no. 8, pp. 2177–2190, 2019.
- [6] J. Liu, J. Guo, and D. Xu, "Geometrymotion-transformer: An end-to-end framework for 3d action recognition," *IEEE Trans. Multimedia*, 2022.

- [7] Z. Wang, L. Zhang, Y. Shen, and Y. Zhou, "D-lio: Tightly-coupled direct lidar-inertial odometry and mapping," *IEEE Trans. Multimedia*, 2022.
- [8] C. R. Qi, H. Su, K. Mo, and L. J. Guibas, "Pointnet: Deep learning on point sets for 3d classification and segmentation," in *Proc. IEEE Conf. Comput. Vis. Pattern Recog.*, 2017, pp. 652–660.
- [9] C. R. Qi, L. Yi, H. Su, and L. J. Guibas, "Pointnet++: Deep hierarchical feature learning on point sets in a metric space," in *Proc. Adv. Neural Inf. Process. Syst.*, 2017, pp. 5105–5114.
- [10] Y. Li, R. Bu, M. Sun, W. Wu, X. Di, and B. Chen, "Pointcnn: Convolution on χ -transformed points," in *Proc. Adv. Neural Inf. Process. Syst.*, 2018, pp. 828–838.
- [11] H. Thomas, C. R. Qi, J.-E. Deschaud, B. Marcotegui, F. Goulette, and L. J. Guibas, "Kpconv: Flexible and deformable convolution for point clouds," in *Proc. IEEE Int. Conf. Comput. Vis.*, 2019, pp. 6411–6420.
- [12] Y. Wang, Y. Sun, Z. Liu, S. E. Sarma, M. M. Bronstein, and J. M. Solomon, "Dynamic graph cnn for learning on point clouds," *ACM Trans. Graph.*, vol. 38, no. 5, pp. 1–12, 2019.
- [13] W. Yuan, T. Khot, D. Held, C. Mertz, and M. Hebert, "PCN: point completion network," in *Int. Conf. 3D Vis.*, 2018, pp. 728–737.
- [14] M. Liu, L. Sheng, S. Yang, J. Shao, and S. Hu, "Morphing and sampling network for dense point cloud completion," in *Proc. AAAI Conf. Artif. Intell.*, 2020, pp. 11 596–11 603.
- [15] X. Yu, Y. Rao, Z. Wang, Z. Liu, J. Lu, and J. Zhou, "PointR: Diverse point cloud completion with geometry-aware transformers," in *Proc. IEEE Int. Conf. Comput. Vis.*, 2021, pp. 12 478–12 487.
- [16] X. Wen, T. Li, Z. Han, and Y. Liu, "Point cloud completion by skip-attention network with hierarchical folding," in *Proc. IEEE Conf. Comput. Vis. Pattern Recog.*, 2020, pp. 1936–1945.
- [17] H. Xie, H. Yao, S. Zhou, J. Mao, S. Zhang, and W. Sun, "Grnet: Gridding residual network for dense point cloud completion," in *Proc. European Conf. Comput. Vis.*, vol. 12354, 2020, pp. 365–381.
- [18] X. Zhang, Y. Feng, S. Li, C. Zou, H. Wan, X. Zhao, Y. Guo, and Y. Gao, "View-guided point cloud completion," in *Proc. IEEE Conf. Comput. Vis. Pattern Recog.*, 2021, pp. 15 890–15 899.
- [19] X. Chen, B. Chen, and N. J. Mitra, "Unpaired point cloud completion on real scans using adversarial training," in *Proc. Int. Conf. Learn. Represent.*, 2020.
- [20] X. Wen, Z. Han, Y. Cao, P. Wan, W. Zheng, and Y. Liu, "Cycle4completion: Unpaired point cloud completion using cycle transformation with missing region coding," in *Proc. IEEE Conf. Comput. Vis. Pattern Recog.*, 2021, pp. 13 080–13 089.
- [21] J. Zhang, X. Chen, Z. Cai, L. Pan, H. Zhao, S. Yi, C. K. Yeo, B. Dai, and C. C. Loy, "Unsupervised 3d shape completion through GAN inversion," in *Proc. IEEE Conf. Comput. Vis. Pattern Recog.*, 2021, pp. 1768–1777.
- [22] Y. Cai, K.-Y. Lin, C. Zhang, Q. Wang, X. Wang, and H. Li, "Learning a structured latent space for unsupervised point cloud completion," in *Proc. IEEE Conf. Comput. Vis. Pattern Recog.*, 2022, pp. 5543–5553.
- [23] R. Wu, X. Chen, Y. Zhuang, and B. Chen, "Multimodal shape completion via conditional generative adversarial networks," in *Proc. European Conf. Comput. Vis.* Springer, 2020, pp. 281–296.
- [24] I. Goodfellow, J. Pouget-Abadie, M. Mirza, B. Xu, D. Warde-Farley, S. Ozair, A. Courville, and Y. Bengio, "Generative adversarial nets," in *Proc. Adv. Neural Inf. Process. Syst.*, vol. 27, 2014, pp. 5543–5553.
- [25] P. Xiang, X. Wen, Y. Liu, Y. Cao, P. Wan, W. Zheng, and Z. Han, "Snowflakenet: Point cloud completion by snowflake point deconvolution with skip-transformer," in *Proc. IEEE Int. Conf. Comput. Vis.*, 2021, pp. 5479–5489.
- [26] Y. Wang, Y. Sun, Z. Liu, S. E. Sarma, M. M. Bronstein, and J. M. Solomon, "Dynamic graph CNN for learning on point clouds," *ACM Trans. Graph.*, vol. 38, no. 5, pp. 146:1–146:12, 2019.
- [27] C. Chen, Z. Han, Y. Liu, and M. Zwicker, "Unsupervised learning of fine structure generation for 3d point clouds by 2d projection matching," in *Proc. IEEE Int. Conf. Comput. Vis.*, 2021, pp. 12 446–12 457.
- [28] A. Dai, C. R. Qi, and M. Nießner, "Shape completion using 3d-encoder-predictor cnns and shape synthesis," in *Proc. IEEE Conf. Comput. Vis. Pattern Recog.*, 2017, pp. 6545–6554.
- [29] X. Han, Z. Li, H. Huang, E. Kalogerakis, and Y. Yu, "High-resolution shape completion using deep neural networks for global structure and local geometry inference," in *Proc. IEEE Int. Conf. Comput. Vis.*, 2017, pp. 85–93.
- [30] D. Stutz and A. Geiger, "Learning 3d shape completion from laser scan data with weak supervision," in *Proc. IEEE Int. Conf. Comput. Vis.*, 2018, pp. 1955–1964.
- [31] Y. Yang, C. Feng, Y. Shen, and D. Tian, "Foldingnet: Point cloud auto-encoder via deep grid deformation," in *Proc. IEEE Conf. Comput. Vis. Pattern Recog.*, 2018, pp. 206–215.
- [32] T. Groueix, M. Fisher, V. G. Kim, B. C. Russell, and M. Aubry, "A papier-mâché approach to learning 3d surface generation," in *Proc. IEEE Conf. Comput. Vis. Pattern Recog.*, 2018, pp. 216–224.
- [33] Y. Tang, Y. Qian, Q. Zhang, Y. Zeng, J. Hou, and X. Zhe, "Warping-gan: Warping multiple uniform priors for adversarial 3d point cloud generation," in *Proc. IEEE Conf. Comput. Vis. Pattern Recog.*, 2022, pp. 6397–6405.
- [34] J. Yang, P. Ahn, D. Kim, H. Lee, and J. Kim, "Progressive seed generation auto-encoder for unsupervised point cloud learning," in *Proc. IEEE Int. Conf. Comput. Vis.*, 2021, pp. 6393–6402.
- [35] J. Pang, D. Li, and D. Tian, "Tearingnet: Point cloud autoencoder to learn topology-friendly representations," in *Proc. IEEE Conf. Comput. Vis. Pattern Recog.*, 2021, pp. 7453–7462.
- [36] L. P. Tchappmi, V. Kosaraju, H. Rezatofghi, I. D. Reid, and S. Savarese, "Topnet: Structural point cloud decoder," in *Proc. IEEE Conf. Comput. Vis. Pattern Recog.*, 2019, pp. 383–392.
- [37] Y. Li, A. W. Yu, T. Meng, B. Caine, J. Ngiam, D. Peng, J. Shen, Y. Lu, D. Zhou, Q. V. Le, A. Yuille, and M. Tan, "Deepfusion: Lidar-camera deep fusion for multimodal 3d object detection," in *Proc. IEEE Conf. Comput. Vis. Pattern Recog.*, 2022, pp. 17 182–17 191.
- [38] P. Sun, H. Kretzschmar, X. Dotiwalla, A. Chouard, V. Patnaik, P. Tsui, J. Guo, Y. Zhou, Y. Chai, B. Caine, V. Vasudevan, W. Han, J. Ngiam, H. Zhao, A. Timofeev, S. Ettinger, M. Krivokon, A. Gao, A. Joshi, Y. Zhang, J. Shlens, Z. Chen, and D. Anguelov, "Scalability in perception for autonomous driving: Waymo open dataset," in *Proc. IEEE Conf. Comput. Vis. Pattern Recog.*, 2020, pp. 2443–2451.
- [39] C. Wang, C. Ma, M. Zhu, and X. Yang, "Pointaugmenting: Cross-modal augmentation for 3d object detection," in *Proc. IEEE Conf. Comput. Vis. Pattern Recog.*, 2021, pp. 11 794–11 803.
- [40] B. Gong, Y. Nie, Y. Lin, X. Han, and Y. Yu, "ME-PCN: point completion conditioned on mask emptiness," in *Proc. IEEE Int. Conf. Comput. Vis.*, 2021, pp. 12 468–12 477.
- [41] H. Zhao, L. Jiang, J. Jia, P. H. Torr, and V. Koltun, "Point transformer," in *Proc. IEEE Int. Conf. Comput. Vis.*, 2021, pp. 16 259–16 268.
- [42] X. Pan, Z. Xia, S. Song, L. E. Li, and G. Huang, "3d object detection with pointformer," in *Proc. IEEE Conf. Comput. Vis. Pattern Recog.*, 2021, pp. 7463–7472.
- [43] M.-H. Guo, J.-X. Cai, Z.-N. Liu, T.-J. Mu, R. R. Martin, and S.-M. Hu, "Pct: Point cloud transformer," *Comput. Visual Media*, vol. 7, no. 2, pp. 187–199, 2021.
- [44] H. Kato, D. Beker, M. Morariu, T. Ando, T. Matsuoka, W. Kehl, and A. Gaidon, "Differentiable rendering: A survey," *CoRR*, vol. abs/2006.12057, 2020.
- [45] O. Wiles, G. Gkioxari, R. Szeliski, and J. Johnson, "Synsin: End-to-end view synthesis from a single image," in *Proc. IEEE Conf. Comput. Vis. Pattern Recog.*, 2020, pp. 7465–7475.
- [46] C. Lin, C. Kong, and S. Lucey, "Learning efficient point cloud generation for dense 3d object reconstruction," in *Proc. AAAI Conf. Artif. Intell.*, 2018, pp. 7114–7121.
- [47] C. Lassner and M. Zollhöfer, "Pulsar: Efficient sphere-based neural rendering," in *Proc. IEEE Conf. Comput. Vis. Pattern Recog.*, 2021, pp. 1440–1449.
- [48] S. Liu, T. Li, W. Chen, and H. Li, "Soft rasterizer: A differentiable renderer for image-based 3d reasoning," in *Proc. IEEE Int. Conf. Comput. Vis.*, 2019.
- [49] N. Ravi, J. Reizenstein, D. Novotný, T. Gordon, W. Lo, J. Johnson, and G. Gkioxari, "Accelerating 3d deep learning with pytorch3d," *CoRR*, vol. abs/2007.08501, 2020.
- [50] N. K. L., P. Mandikal, M. Agarwal, and R. V. Babu, "Capnet: Continuous approximation projection for 3d point cloud reconstruction using 2d supervision," in *Proc. AAAI Conf. Artif. Intell.*, 2019, pp. 8819–8826.
- [51] N. K. L., P. Mandikal, V. Jampani, and R. V. Babu, "DIFFER: moving beyond 3d reconstruction with differentiable feature rendering," in *Proc. IEEE Conf. Comput. Vis. Pattern Recog. Workshops*, 2019, pp. 18–24.
- [52] Z. Han, C. Chen, Y. Liu, and M. Zwicker, "DRWR: A differentiable renderer without rendering for unsupervised 3d structure learning from silhouette images," in *Proc. Int. Conf. Mach. Learn.*, vol. 119, 2020, pp. 3994–4005.
- [53] S. Suzuki *et al.*, "Topological structural analysis of digitized binary images by border following," *Comput. Vision, Graphics, and Image Process.*, vol. 30, no. 1, pp. 32–46, 1985.
- [54] E. Insafutdinov and A. Dosovitskiy, "Unsupervised learning of shape and pose with differentiable point clouds," *Proc. Adv. Neural Inf. Process. Syst.*, vol. 31, 2018.
- [55] Q. Xu, W. Wang, D. Ceylan, R. Mech, and U. Neumann, "Disn: Deep implicit surface network for high-quality single-view 3d reconstruction," *Proc. Adv. Neural Inf. Process. Syst.*, vol. 32, 2019.

- [56] A. X. Chang, T. Funkhouser, L. Guibas, P. Hanrahan, Q. Huang, Z. Li, S. Savarese, M. Savva, S. Song, H. Su *et al.*, “Shapenet: An information-rich 3d model repository,” *arXiv preprint arXiv:1512.03012*, 2015.
- [57] A. Geiger, P. Lenz, and R. Urtasun, “Are we ready for autonomous driving? the kitti vision benchmark suite,” in *Proc. IEEE Conf. Comput. Vis. Pattern Recog.* IEEE, 2012, pp. 3354–3361.
- [58] L. Qi, L. Jiang, S. Liu, X. Shen, and J. Jia, “Amodal instance segmentation with KINS dataset,” in *Proc. IEEE Conf. Comput. Vis. Pattern Recog.*, 2019, pp. 3014–3023.